arXiv:astro-ph/0504444v2 27 Jul 2005

The pressure distribution in thermally bistable turbulent flows

Adriana Gazol[1], Enrique Vázquez-Semadeni[1]

Centro de Radioastronomía y Astrofísica, UNAM, A. P. 3-72, c.p. 58089, Morelia, Michoacán, México

a.gazol@astrosmo.unam.mx e.vazquez@astrosmo.unam.mx

and

Jongsoo Kim[2]

Korea Astronomy and Space Science Institute, 61-1, Hwaam-Dong, Yusong-Ku Taejon 305-348, Korea

jskim@kasi.re.kr

ABSTRACT

We present a systematic numerical study of the effect of turbulent velocity fluctuations on the thermal pressure distribution in thermally bistable flows. The turbulent fluctuations are characterized by their rms Mach number M (with respect to the warm medium) and the energy injection wavenumber, $k_{\rm for} = 1/\ell$, where ℓ is the injection size scale in units of the box size L =100 pc. The numerical simulations employ random turbulent driving generated in Fourier space rather than star-like heating, in order to allow for precise control of the parameters. Our range of parameters is $0.5 \leq M \leq 1.25$ and $2 \leq k_{\rm for} \leq 16$. Our results are consistent with the picture that as either of these parameters is increased, the local ratio of turbulent crossing time to cooling time decreases, causing transient structures in which the effective behavior is intermediate between the thermal-equilibrium and adiabatic regimes. As a result, the effective polytropic exponent $\gamma_{\rm e}$ of the simulations ranges between ~ 0.2 to ~ 1.1, and the mean pressure of the diffuse gas is generally reduced below the thermal equilibrium pressure $P_{\rm eq}$, while that of the dense gas is increased with respect to $P_{\rm eq}$. The fraction of high-density zones ($n > 7.1$ cm^{-3}) with $P > 10^4$ K cm^{-3} increases from roughly 0.1% at $k_{\rm for} = 2$ and $M = 0.5$ to roughly 70% for $k_{\rm for} = 16$ and $M = 1.25$. A preliminary comparison with the recent pressure measurements of Jenkins (2004) in CI favors our case with $M = 0.5$ and $k_{\rm for} = 2$. In all cases, the dynamic range of the pressure in any given density interval is larger than one order of

magnitude, and the total dynamic range, summed over the entire density range, typically spans 3–4 orders of magnitude. The total pressure histogram widens as the Mach number is increased, and moreover develops near-power-law tails at high (resp. low) pressures when $\gamma_e \lesssim 0.5$ (resp. $\gamma_e \gtrsim 1$), which occurs at $k_{for} = 2$ (resp. $k_{for} = 16$) in our simulations. The opposite side of the pressure histogram decays rapidly, in an approximately lognormal form. This behavior resembles that of the corresponding density histograms, in spite of the large scatter of the pressure in any given density interval. Our results show that turbulent advection alone can generate large pressure scatters, with power-law high-P tails for large-scale driving, and provide validation for approaches attempting to derive the shape of the pressure histogram through a change of variable from the known form of the density histogram, such as that performed by Mac Low et al. (2004).

Subject headings: ISM: structure — instabilities — turbulence — hydrodynamics — ISM: kinematics and dynamics

1. Introduction

The atomic interstellar medium (ISM) is generally believed to be thermally bistable. This property arises because the neutral gas is thermally unstable for 300 K $\lesssim T \lesssim$ 5000 K under the isobaric mode of thermal instability (TI; Field 1965; see also the review by Meerson 1996), allowing for a configuration in which gas with temperatures above and below this range can coexist in thermal pressure equilibrium (Field, Goldsmith & Habing 1969; Wolfire et al. 1995, 2003), being mediated by a thin interface of thickness comparable to the conductive length (Begelman & McKee 1990). This tendency of the HI gas to naturally segregate in two phases has long been thought to be the dominant mechanism in forming and maintaining cold cloudlets of sizes ~ 0.1 pc confined by the thermal pressure of a warm, dilute substrate.

On the other hand, the ISM is known to be globally turbulent, with numerous kinds of energy sources acting on a wide range of scales (e.g., Scalo 1987; Norman & Ferrara 1996), including spiral arm shocks, large-scale combined instabilities, supernova and HII-region energy input, etc. (see, e.g., Mac Low & Klessen 2004 for a review). The net effect is to produce and maintain a turbulent velocity dispersion that is transonic with respect to the warm gas, and supersonic with respect to the cold medium (e.g., Heiles & Troland 2003).

In recent years the interplay between TI and turbulence has been studied by several groups. Some of the main issues are: The development and signatures of TI in a turbulent ISM (e.g. Vázquez-Semadeni, Gazol & Scalo 2000; Sánchez-Salcedo, Vázquez-Semadeni &

Gazol 2002; Vázquez-Semadeni et al. 2003), the triggering of TI by strong compressions in the warm medium (Hennebelle & Pérault 1999, 2000), the generation of turbulence at the nonlinear stages of development of TI (Koyama & Inutsuka 2002; Kritsuk & Norman 2002), the production and maintenance of small-scale cold structures (Burkert & Lin 2000; Koyama & Inutsuka 2000, 2002; Audit & Hennebelle 2005), the interaction between TI and magneto-rotational instability (Piontek & Ostriker 2004) the production and maintenance of significant amouts of gas at thermally unstable temperatures (Gazol et al. 2001; Audit & Hennebelle 2004), as motivated by the reports of several observational studies (Dickey, Salpeter & Terzian 1977; Kalberla, Schwarz & Goss 1985; Spitzer & Fitzpatrick 1995; Fitzpatrick & Spitzer 1997; Heiles 2001; Heiles & Troland 2003; Kanekar et al. 2003), and the thermal pressure distribution in the turbulent ISM (Audit & Hennebelle 2004; de Avillez & Breitschwerdt 2004; Mac Low et al. 2004; see also Vázquez-Semadeni et al. 1995; Korpi et al. 1999 for discussions of cases without thermal bistability.)

Physical discussions of the effect of turbulent velocity fluctuations in a thermally bistable medium have been given by Sánchez-Salcedo & al. (2002), Vázquez-Semadeni et al. (2003), Wolfire et al. (2003), and Audit & Hennebelle (2004). The first two of these works noted that velocity fluctuations induce perturbations on the gas that can range from behaving adiabatically, when the turbulent crossing time $\tau_{\rm t}$ across the perturbation size scale is much shorter than the cooling time $\tau_{\rm c}$, to behaving according to the thermal equilibrium condition between cooling and heating, in the opposite limit. The turbulent crossing time, in turn, depends on the scale and amplitude of the velocity fluctuations, and therefore the higher the Mach number, or the smaller the typical scale of the turbulence, the higher the fraction of fluid parcels that are expected to transiently behave closer to an adiabatic regime, and farther away from thermal equilibrium. Sánchez-Salcedo & al. (2002) and Vázquez-Semadeni et al. (2003) used this to explain the presence of significant amounts of gas with temperatures corresponding to the unstable range. Audit & Hennebelle (2004) have further quantified the problem by producing a semi-analytical model that follows the stretching of a fluid parcel due to the shearing components of the turbulence while it seeks thermal equilibrium, to give a relation between the amplitude of this component and the amount of thermally unstable gas present in the flow. Finally, Wolfire et al. (2003) have given an estimate of the ratio η of the turbulent crossing time to the cooling time in the warm neutral medium, finding values 0.3–0.9, which led them to suggest that this medium should often exhibit non-equilibrium temperatures.

These results have implications for the thermal pressure PDF in the flow. As a fluid parcel departs from thermal equilibrium, its pressure also departs from the equilibrium value, and we expect a *distribution* of the thermal pressure around its thermal equilibrium value at a given density, determined by the distribution of Mach numbers of the velocity fluctuations.

This holds even in the absence of direct local heating.

The thermal pressure probability density function (PDF) varies significantly among different models of the ISM. In the simplest equilibrium multiphase model (Field et al. 1969), the thermal pressure PDF is simply a delta function at the mean value of the pressure in the midplane. If this value encompasses the unstable range, then the medium is expected to be segregated into the two phases, both at the mean, equilibrium pressure, but with densities and temperatures bracketing the unstable range. The next level of complexity was added by including supernova heating (Cox & Smith 1974; McKee & Ostriker 1977). In particular, the McKee & Ostriker (1977) model implied a piecewise power-law pressure PDF (Jenkins, Jura & Lowenstein 1983; see also Mac Low et al. 2004) with slope $-19/9$ for $P \leq P_c$ and $-23/9$ for $P > P_c$, where $P_c/k = 10^{3.67}$ cm^{-3}K. Moreover, the model predicted no pressures below the equilibrium pressure of the warm and cold phases. This distribution, however, follows from a consideration of the probability of a given point in space belonging to a hot supernova remnant, and the theoretical evolution of these remnants, not from a consideration of the local thermodynamic changes in the gas due to the turbulent compressions and rarefactions (advection) that are induced by the supernova energy injection.

Inclusion of advection is naturally accomplished in numerical models of the star-driven ISM (see Vázquez-Semadeni 2002 for a review). In particular, the recent papers by Mac Low et al. (2004) and de Avillez & Breitschwerdt (2004) have discussed the pressure PDF resulting in their simulations, albeit they appear to obtain different functional forms for it: Mac Low et al. find a lognormal PDF, while de Avillez & Breitschwerdt find PDFs that appear closer to a power law, with a slope in fact not too different from that predicted by McKee & Ostriker (1977). From the lognormal shape of their PDF, Mac Low et al. conclude that it originates from the density PDF for an isothermal turbulent flow. However, in those simulations it is not possible to disentangle the pressure fluctuations induced purely by turbulent motions, and those due to direct heating from nearby stellar sources.

Observationally, significant pressure fluctuations have been reported in the cold medium. Jenkins et al. (1983) found, using *Copernicus* observations of CI, variations greater than an order of magnitude in the cold gas pressure with small amounts of gas at up to $P/k = 10^5$ K cm^{-3}. More recently, Jenkins & Tripp (2001) used the *Space Telescope Imaging Spectrograph* (*STIS*) to confirm this result with better resolved data. Additionally they found that their results implied an effective polytropic index for the cold gas $\gamma > 0.9$, which is larger than the $\gamma = 0.72$ derived by Wolfire et al. (1995) for cold gas at thermal equilibrium, mentioning that this could be due to the fact that compressed regions may have a cooling time larger than the dynamical time, so it may behave closer to adiabatically. Finally, it is well known that in the local ISM there is an apparent pressure imbalance between the hot

($T \sim 10^6$K, $P/k_b \sim 11,000$K cm^{-3}) and the warm ($T \sim 6,700$K, $P/k_b \sim 2,300$K cm^{-3}) gas (see e.g. Jenkins 2002; Redfield & Linsky 2004).

In this paper, we present a systematic study aimed at investigating in detail the effects of turbulent velocity fluctuations on a thermally bistable flow, in particular on the transition from nearly-adiabatic to near-thermal equilibrium behavior, and on the PDF of thermal pressure. The simulations we present here are not intended as accurate models of the ISM, but instead as numerical experiments allowing us to clearly identify the effects of two fundamental turbulent parameters, the rms Mach number M and the energy injection scale (characterized by its wavenumber $k_{\rm for}$), on the thermodynamic response of a thermally bistable flow. For this reason, we have opted for using Fourier random driving, trading up realism for accurate control of these parameters, and consider non-magnetic, non-self-gravitating flows. Also, in order to allow for the large number of simulations needed to cover a significant range in parameter space, we have restricted most of the simulations to two dimensions, although we present a few selected cases in three dimensions (3D) in order to check that the main trends observed the two-dimensional runs are preserved in 3D.

The outline of the paper is as follows. In §2 we describe the model used for the simulations and its limitations, and in §3, we present convergence tests for this model. In §4 we then present the main results, concerning the effective thermodynamic behavior of the flow and the pressure PDF, both in global form and in specific density intervals, as the parameters M (§4.1) and $k_{\rm for}$ (§4.2) are varied. Then, in §5 we discuss these results in the context of the simple physical scenario of a transition from near–thermal-equilibrium to near-adiabaticity (§5.1), we show persistence of the main trends in 3D (§5.2), and we discuss some implications of our results for previous models and simulations (§5.3). Finally, in §6 we give a summary and some conclusions.

2. The Model

2.1. Prescription

We solve the hydrodynamic equations, including the energy equation, to simulate a region of 100 pc on a side, with periodic boundary conditions. The simulations discussed in this paper are in two dimensions (2D) except for those described in §5.2.

The equations are solved by means of a MUSCL-type scheme (Monotone Upstream-centered Scheme for Conservation Laws) with HLL Riemann solvers (Harten, Lax, & van Leer 1983; Toro 1999), augmented with model terms for radiative cooling and background heating, and a prescription for random turbulent forcing. The background heating is taken

as a constant $\Gamma_0 = 2.51 \times 10^{-26}$erg s^{-1}H^{-1}, where "H^{-1}" means "per Hydrogen atom". This is the value of the photo-electric heating rate at density $n = 1$ cm^{-3} reported by Wolfire et al. (1995), and is roughly within half an order of magnitude of its value throughout the range 10^{-2}cm$^{-3} \leq n \leq 10^{3}$cm^{-3}, as reported by those authors. We then use this value to fit the "standard" equilibrium P vs. ρ curve of Wolfire et al. (1995) assuming that the background heating is in equilibrium with a cooling function that has a piece-wise power-law dependence on the temperature. We find (Sánchez-Salcedo et al. 2002)

$$\Lambda = \left\{ \begin{array}{ll} 0 & T < 15\ K \\ 3.42 \times 10^{16} T^{2.13} & 15\ K \leq T < 141\ K \\ 9.10 \times 10^{18} T & 141\ K \leq T < 313\ K \\ 1.11 \times 10^{20} T^{0.565} & 313\ K \leq T < 6101\ K \\ 2.00 \times 10^{8} T^{3.67} & 6101\ K \leq T \end{array} \right\} \quad (1)$$

where the coefficients have units of erg s^{-1}g^{-2}cm^{3}K$^{-\beta}$, with β being the temperature exponent in the corresponding interval. Under thermal equilibrium conditions, the gas is thermally unstable under the isobaric mode for 313 K $< T <$ 6102 K, and marginally stable for 141 K $< T <$ 313 K. In thermal equilibrium, the transition temperatures $T = 6102$, 313 and 141 K correspond to densities $n = 0.60$, 3.2 and 7.1 cm^{-3}, respectively.

The turbulent driving is 100% solenoidal, and is done in Fourier space at a specified narrow two- or three-dimensional wavenumber band, $k_{\rm for} - 1 \leq k \leq k_{\rm for}$, where $k \equiv \sqrt{k_x^2 + k_y^2}$ in 2D and $k \equiv \sqrt{k_x^2 + k_y^2 + k_z^2}$ in 3D, and with the Gaussian deviates having zero mean and unitary standard deviation. The amplitude of velocity perturbations is fixed by a constant injection rate of kinetic energy as in the prescription of Mac Low (1999), although with the difference that we use a different random seed at each driving time. The kinetic energy input rate is chosen as to approximately maintain a desired sonic Mach number.

In the set of simulations presented in §4, the fluid is initially at rest and has a uniform density ($n_0 = 1$ cm^{-3}) and temperature ($T_0 = 2399$ K), so that, in the absence of turbulence, the medium would spontaneously segregate into warm-diffuse ($n = 0.34$ cm^{-3}, $T = 7104$ K) and cold-dense ($n = 37.2$ cm^{-3}, $T = 64.5$ K) phases. The time unit t_0 is chosen to be the sound crossing time across the numerical box at a speed of 9.1 km s^{-1}, corresponding to the isothermal sound speed at 10^4 K. Thus, $t_0 = 10.8$ Myr. Mach numbers are expressed with respect to this sound speed.

For the parameters we use as initial conditions, and in the presence of realistic thermal conductivity (see §3), the maximum linear growth rate occurs at scales ~ 8.3 pc, while the so called Field length (the minimum unstable scale) is 0.7 pc. In our simulations, thermal conductivity is not included, other than the numerical diffusion caused by the finite-differencing. This causes a "numerical Field length" ~ 3 pc in simulations at a resolution

of 512^2, with the maximum growth rate occurring at scales between 12.5 and 25 pc, as determined through the tests described in §3. Thus, the unstable wavelength range in our simulations is somewhat more compressed than the real unstable range in the linear regime. We discuss the neglect of thermal conductivity further in §2.2.2, and resolution issues in §3.

2.2. Features and limitations of the model

2.2.1. Random Fourier driving

In the simulations presented here, the turbulence is driven using a random scheme executed in Fourier space. This means that every point in physical space is subject to a force at any given time. This is not a very realistic way of driving the turbulence, as in the real ISM the driving sources, such as supernova explosions or spiral-arm shock waves are localized in space. Nevertheless, turbulence is expected to "propagate away" from the localized sources (Avila-Reese & Vázquez-Semadeni 2001), generating a general turbulent flow. More importantly, we choose this form of driving because of two reasons. First, it allows us to precisely control the scale of energy injection as well as the rms Mach number in the flow. This is very important, because one of our motivations is to test the scenario described in Sánchez-Salcedo et al. (2002) and Vázquez-Semadeni et al. (2003) that velocity fluctuations behave closer to an adiabatic regime as the turbulent crossing time becomes shorter than the cooling time, and the turbulent crossing time is directly a function of the scale size and amplitude of the velocity perturbations.

The second reason is that random Fourier driving guarantees that all pressure fluctuations that develop are caused purely by advection (fluid transport) and not by direct injection of heat by stellar sources, allowing us to isolate the effects of velocity fluctuations on the pressure distribution. This implies that the widths of the pressure distributions in our simulations should constitute a lower limit to the actual widths expected in the actual ISM, in which the energy is injected as heat by stellar sources, directly raising the local pressure, in addition to any effects of the turbulent advection.

2.2.2. Neglect of thermal conductivity

The equations solved in our simulations do not include a model term for the thermal conductivity. Koyama & Inutsuka (2004) have suggested that thermal conductivity should always be included in numerical simulations of thermally unstable flows, and that enough resolution to resolve the so called "Field length" (Field 1965; Begelman & McKee 1990)

should be always be used, because of mainly two reasons. First, if no thermal conduction at all is included, then the TI growth rate asymptotically approaches its maximum value as the perturbation length scale approaches zero. This means that, in a finite-resolution numerical grid, the smallest resolved scale is maximally unstable, regardless of the resolution used, creating numerical problems. However, in practice this does not occur, as the numerical diffusion of the code creates a "numerical Field length", that is, a minimum unstable scale larger than the grid cell size, even if it does not have the same functional temperature dependence as the actual Field length. Indeed, we have verified that density perturbations of amplitude 2.5% and wavelength $\lambda = 16$ pixels (3.1 pc) in a simulation of resolution 512^2 remain stationary (thus being the "numerical Field length"), while pertubations with $\lambda = 4$ pixels (0.8 pc) are completely damped in times ~ 3 Myr. This timescale is comparable to the e-folding time of the growing modes described in §3. Thus, numerical diffusion adequately prevents instability of the smallest resolved scales. Because of the very small wavelength, numerical dissipation is more effective than TI, which results in damping rather than growing of the perturbation.

Note that Koyama & Inutsuka (2004) also warned that if no realistic thermal conductivity is employed, then the results are resolution-dependent, because the characteristic scale of numerical diffusion depends on the resolution. Thus, they concluded that, in order to have numerically converged results in the presence of TI, one should i) include an explicit conduction term that is larger than the conduction due to numerical diffusion, ii) use a cell size that is smaller than one third of the conductive Field length. However, for the *global* properties that interest us here, such as PDFs of thermal pressure and density, the difference between the effects of numerical diffusion and of an explicit conduction term, whose associated Field length is comparable or smaller than the cell size, is probably not significant. Indeed, in §3 we show that our simulations are perfectly converged at high densities and pressures (which is normally the regime of most concern; e.g., Audit & Hennebelle 2004) at the resolution we use.

The second warning of Koyama & Inutsuka (2004) refers to the possibility of missing dynamical effects originating from the effects of the thermal conduction. Specifically, they describe the generation of motions with Mach numbers up to 0.13 due to the pressure gradients generated by the conductivity. Moreover, in their simulations of the development of TI alone, these motions cause the resulting condensations to coalesce, so that at the end of the simulation the number of condensations has decreased by almost a factor of 2. However, Koyama & Inutsuka (2004) noted that the initial number of condensations formed in their simulations was determined by the initial fluctuations, not by the inclusion or omission of thermal conductivity. In addition, the Mach numbers generated in their simulations are at least 5 times smaller than those of the smallest turbulent motions we impose on the flow, and

therefore, in our simulations, density fluctuation production and coalescence is dominated by the turbulent velocity fluctuations, not by TI in the presence of thermal conductivity. Thus, for our purposes, the motions produced by thermal conductivity can be neglected.

3. Convergence test

Here we present results from 20 simulations tailored to investigate the convergence of the model described in §2.

We first consider the linear regime. In figure 1 we show the temporal growth of sinusoidal density perturbations with an initial amplitude of 2.5%. The spatial period of these perturbations is 50 pc (*upper left panel*), 25 pc (*upper right panel*), 12.5 pc (*lower left panel*) and 6.25 pc (*lower right panel*), respectively corresponding to wave-numbers ($k_{\rm p}$) of 2, 4, 8 and 16 respectively. The solid, dotted and dashed lines are for resolutions of $N = 256^2$, 512^2 and 1024^2, respectively. The thick line in each frame indicates the theoretical growth rate at the corresponding scale. To obtain this slope, we have solved the dispersion relation (Field 1965) using the cooling function described above (eq. (1)) and a realistic, although temperature-independent, value of the conductivity $K = K_0 = 5/3(k_b T_0 l/v_{\rm rms})n_0(3k_b/2m)$ (Lang 1999), where k_b is Boltzmann's constant, and we have taken $T_0 = 2400$K, $n_0 = 1$ cm^{-3}, $m = m_H$, $l = 3.2 \times 10^{-3}$pc and $v_{\rm rms} = 5.7$ km s^{-1}, the adiabatic sound speed at T_0. These simulations are initially at rest and have a uniform temperature of $T_0 = 2400$K. It can be seen that for $k_{\rm p} = 2$, 4, and 8 the linear growth rate of the perturbations in the simulations at all three resolutions is in good agreement with the theoretical growth rate. For $k_{\rm p} = 16$, we see that the run with $N = 512$ has nearly converged to the correct growth rate, while the run with $N = 256$ severely damps the growth of this mode. We conclude that a resolution $N = 512$ is an acceptable resolution for capturing the linear growth, in the presence of realistic conductivity, of modes with sizes down to 1/16 the box size.

We now turn to the nonlinear case, which is the most relevant one for the driven-turbulence simulations presented in this paper. In figure 2 we display the temporal growth of sinusoidal density perturbations with an initial amplitude of 2.5% for simulations with sinusoidal large-amplitude (Mach number 1.0 with respect to the unperturbed medium) velocity perturbations. The velocity and density perturbations are in phase, with wavelengths 6.25 pc (*left*) and 12.5 pc (*right*). In this case the comparison with the theoretical growth rate is not meaningful. However, it can be seen that the difference between the growth rates for $N = 512$ and $N = 1024$ at $k_p = 16$ is smaller than for the pure density perturbation case.

As a final test, we compare the total time-averaged (from 1.1 to 2 simulation sound

crossing times) pressure and density histograms for two fully turbulent simulations with driving wavenumber $k_{\rm for} = 2$ and rms Mach number $M = 1$, at resolutions of 512^2 and 1024^2 (fig. 3). We see that the right sides (high values) of the histograms are perfectly converged at 512^2, while the left sides (low values) are approximately so, with the same relative number of points as the 1024^2 run in density and pressure intervals within a factor of 3 from the histogram maximum, and deviations by factors no larger than ~ 3 in more distant density or pressure intervals. From all of the above results, we therefore adopt $N = 512$ as a compromise between acceptable resolution, and the ability to perform the numerous simulations needed for this study.

Note that with a box of 100 pc on each side and $N = 512$, the smallest resolved scale, even neglecting the effects of numerical diffusion, is ~ 0.2 pc. This is larger than the typical size (~ 0.1 pc) of the cold structures generated by TI and thus our simulations probably overestimate the sizes of those cloudlets that are formed by the instability rather than by larger-scale, coherent turbulent compressions, and certainly do not resolve their internal structure. However, our interest here is in statistical quantities, such as the distribution of the pressure values at every density interval, and the fraction of the volume occupied by gas with a given pressure. The fact that the high-value sides of the density and pressure histograms at 512^2 and 1024^2 resolutions are nearly identical suggests that this information deos not require resolving the tiniest structures, and is accurately captured by our simulations.

4. Results

We now describe the results of 10 simulations aimed at characterizing the effect of velocity fluctuations on the thermal pressure distribution in a thermally bistable flow. The simulations analyzed in the next two sections are performed in 2D, with a resolution of 512 grid points per dimension, whereas the simulations described in §5.2 are performed in two and three dimensions, with 256 grid points in each direction. The forcing is applied at wavenumbers of $k_{\rm for} = 2$, 4, 8 and 16, implying a driving scale of 50, 25, 12.5 and 6.25 pc respectively, and has the necessary amplitude to induce turbulent motions with rms Mach numbers $M \sim 0.5$, 1.0 and 1.25. This is intended to represent realistic values of the Mach number in the warm phase. Of course, actual local Mach numbers can be much higher, as the temperature is generally lower in higher density gas.

Initially, all our simulations are at rest and have a uniform density ($n_0 = 1$ cm^{-3}) and temperature ($T_0 = 2400$K). In order to allow the simulations to reach a stationary regime, we evolve the simulations for at least two crossing times across the turbulence driving scale, given by $t_0/Mk_{\rm for}$. Specifically, cases with $k_{\rm for} \geq 4$ are evolved for two code time units ($2t_0$),

while those with $k_{\rm for} = 2$ are evolved for $4t_0$. These times represent several cooling times at T_0, given by

$$\tau_{\rm cool} = \frac{c_{\rm v} T}{\rho_{\rm eq} \Lambda(T)} = 6.27 \times 10^5 \ {\rm yr},$$

where $c_{\rm V}$ is the specific heat at constant volume and $\rho_{\rm eq}$ is the unstable equilibrium density.

4.1. The effect of the driving scale

We first discuss the response of the pressure to changes in the driving wavenumber $k_{\rm for}$, and so in this section we restrict ourselves to rms Mach numbers $M \approx 1$. Recalling that M is not directly an input parameter of the simulations, but a result of the energy input rate, the actual value of M differs slightly from the target value. Specifically, its actual values are $M = 0.97$, 0.96, 0.92 and 0.95 for the runs with $k_{\rm for} = 2$, 4, 8 and 16, respectively.

Figure 4 shows two-dimensional histograms for these runs, giving the number of grid points in the simulation in a given (P, n) bin. The contours are logarithmic and are set at 10%, 30%, 50%, 70% and 90% of the $\log_{10}$ of the maximum value of the two-dimensional histogram for each simulation. The histograms are computed at $t = 1.5t_0$ (resp. $t = 3.0t_0$) for simulations with $k_{\rm for} > 2$ (resp. $k_{\rm for} = 2$). It is clearly seen that as the driving scale decreases ($k_{\rm for}$ increases), the distribution of points shifts away from the thermal equilibrium curve (denoted by the broken solid line), and towards adiabatic behavior (with slope 5/3). It is also seen that at low densities a substantial fraction of the points lies *below* the thermal equilibrium curve. That is, they have probably been cooled by negative $P\ dV$ work, and have not had time yet to warm back up by the background heating. Finally, an interesting branch of points seems to lie on the extension of the equilibrium curve for the dense gas, but at densities corresponding to the diffuse gas.

These trends can also be seen in figure 5, which shows temporally-averaged pressure histograms computed in three density ranges $n_c/\sqrt{2} \leq n_c < \sqrt{2} n_c$, with $n_c = 0.1$, 1.0 and 10.0 cm^{-3}, corresponding to the warm, unstable and cold ranges. It can be seen that for low densities the most probable pressure $P(N_{\rm max})$ is in general *lower* than the thermal equilibrium pressure at n_c ($P_{\rm eq}$, denoted in the figure by the vertical lines), and shifts progressively farther away from it as $k_{\rm for}$ increases. At densities corresponding to the thermally unstable range, the most probable pressure increases with increasing $k_{\rm for}$, and passes from being smaller to being larger than $P_{\rm eq}$. Finally, at $n_c = 10.0$ cm^{-3}, the four histograms peak close to $P_{\rm eq}$, although the height decreases rapidly with increasing $k_{\rm for}$. Moreover, a high-pressure tail is present, which becomes more populated and more extended as $k_{\rm for}$ is increased. Finally, we note that, in all histograms displayed in figure 5, the dynamic range is larger than

an order of magnitude.

The time-averaged pressure and density histograms for the whole field of all the simulations in this group are shown in figure 6. The pressure histograms span 3–4 orders of magnitude, with both their width and $P(N_{\rm max})$ increasing as $k_{\rm for}$ increases. Also, the histograms become more skewed, lifting their low-P side. The density histograms are bimodal, but as $k_{\rm for}$ increases, the bimodality becomes less pronounced and the histogram becomes narrower.

4.2. The effect of the Mach number

We now turn to the effect of the rms Mach number on the pressure distribution. To this effect, in this section we present results from two sets of three simulations each, with $M \sim 0.5$, 1.0 and 1.25, and $k_{\rm for} = 2$ and 16. The actual values of M in these simulations are $M = 0.50$, 0.97 and 1.25 at $k_{\rm for} = 2$, and $M = 0.56$, 0.95 and 1.25 at $k_{\rm for} = 16$.

The two-dimensional histograms in the pressure-density space are shown in figures 7 and 8 for $k_{\rm for} = 2$ and 16, respectively. The contours are set at the same levels as in §4.1. The dynamic range of both density and pressure is seen to increase with increasing M for both driving scales. For $k_{\rm for} = 2$, a slight variation of the mean slope of the distribution of points can be easily seen, while a clear steepening of the mean slope is observed at $k_{\rm for} = 16$. This variation is summarized in fig. 13 for all runs. Finally, the tendency of the pressure distribution to shift away from thermal equilibrium for smaller driving scales, reported in the previous section, is seen for all three values of M.

The pressure histograms for specific density intervals show a variety of behaviors. For $k_{\rm for} = 2$ (fig. 9), the histogram centered on $n_c = 0.1$ cm^{-3} shifts from being narrow and peaking very close to $P_{\rm eq}$ at $M = 0.5$ to a wider distribution peaking below $P_{\rm eq}$ at $M = 1$ and 1.25. The histograms for the unstable gas at $n_c = 1$ exhibit almost no shift of their peak $P(N_{\rm max})$, which is located a half order of magnitude below $P_{\rm eq}$, as M is increased, although the high-P tail becomes higher, with a shallower slope, and extends to higher pressures. In the high-n range, the histograms show almost no change in $P(N_{\rm max})$, but the high-P tail becomes progressively shallower, and extends up to higher values, as M is increased.

For $k_{\rm for} = 16$ (fig. 10), the histograms at $n_c = 0.1$ cm^{-3} and $n_c = 1$ cm^{-3} show little variation in shape and in $P(N_{\rm max})$, although the histogram at $n_c = 0.1$ almost doubles its height, indicating that a higher fraction of the volume in the simulation is occupied by diffuse gas as M is increased. This is compensated by a decrease in the volume occupied by the dense, $n_c = 10$ cm^{-3} gas, which moreover experiences an increment of roughly one and a

half orders of magnitude in its typical pressure $P(N_{\rm max})$.

In the pressure histograms for the whole simulations (fig. 11 *left*) at $k_{\rm for} = 2$, the different behavior between the run with $M \sim 0.5$ and those with $M \sim 1.0$ and $M \sim 1.25$ is also evident. In the former case the histogram is narrower and close to lognormal, although with a high-P tail for $P \gtrsim 10^4$ K cm^{-3}. As M increases, $P(N_{\rm max})$ shifts to slightly lower pressures, and the high-P tail reaches closer to the histogram peak, lifting the entire high-P side of the histogram and causing it to approximate a power law. On the other hand, the low-P side of the histogram widens with increasing M, but never seems to lose its approximately lognormal shape.

In the density histograms for $k_{\rm for} = 2$ (fig. 11 *right*), the distinction between $M \sim 0.5$ and the other two cases is also noticeable. The bimodal shape of the histogram becomes less pronounced as M is increased, with $n(N_{\rm max})$ shifting slightly towards lower densities. The histogram width increases with increasing M, at least in the range explored.

For $k_{\rm for} = 16$ (fig. 12, *left*), the high-P branch in the pressure histogram decays faster than the low pressure one at all values of M, and its slope is almost independent of M, although $P(N_{\rm max})$ shifts to higher pressures. In this case again the histogram becomes broader with increasing M, but mainly because the low-P tail is lifted and extends to lower pressures.

Concerning the density histograms, similarly to the case with $k_{\rm for} = 2$, for $k_{\rm for} = 16$, an increase in M leads to a less bimodal density histogram (fig. 12, *right*), but in this case, the histogram broadens with increasing M, although mainly by lifting its low-n tail. A comparison between the density histograms shown in figures 11 and 12 confirms the fact, discussed in previous section, that the density distribution becomes narrower with increasing $k_{\rm for}$.

5. Discussion

5.1. A unified physical picture

The main results of §4 can be summarized as follows: (1) The distribution of points in the P-n diagram widens and steepens as either M or $k_{\rm for}$ are increased. (2) The mean pressure in a given density interval drifts away from the equilibrium value $P_{\rm eq}$ as $k_{\rm for}$ is increased, moving towards $P > P_{\rm eq}$ for the dense gas, and towards $P < P_{\rm eq}$ for the diffuse gas. (3) The pressure histograms in these density ranges as well as the global pressure histograms are generally skewed, and tend to reverse their skewness with increasing $k_{\rm for}$. (4)

The pressure histograms in specific density ranges increase their width as M is increased. (5) The global pressure histograms develop one near-power-law side and one near-lognormal side. For low $k_{\rm for}$, the near-power-law develops on the high-P side, while for high $k_{\rm for}$ the near-power-law side develops at low P. In general, the slope of the power law flattens as M is increased.

Most of these results can be understood simply as a consequence of the turbulent crossing time becoming shorter in local compressions as either the Mach number M or the driving wavenumber $k_{\rm for}$ are increased, creating a larger fraction of compressions that evolve closer to adiabatically, and thus temporarily drift away from thermal equilibrium. Indeed, for our choice of parameters, the cooling and sound crossing times in the unstable gas are equal at a scale $\lambda_{\rm eq} \sim 4$ pc. For the warm medium in thermal equilibrium, this scale increases to ~ 23 pc. The scale $\lambda_{\rm eq}$ also applies for equality of the turbulent crossing time and the cooling time for Mach-1 motions. Below this scale, classical isobaric perturbations would evolve nearly isobarically, because condensation occurs on roughly the cooling time, which is longer than the time needed to restore pressure balance (the sound crossing time). However, velocity perturbations below this scale generate perturbations that approach adiabatic behavior as their Mach number increases, because in this case the externally-applied turbulent compression exerts PdV work on the fluid parcel, heating it on timescales shorter than the cooling time. Adiabatic perturbations are stable to first order (Field 1965), and imply that the pressure *increases* with increasing density. The net behavior in transonic flows is expected to be intermediate between thermal equilibrium and adiabaticity.

The tendency towards adiabatic behavior causes a progressive increase in the slope (or effective polytropic exponent, $\gamma_{\rm e}$) of the ensemble of points in the P-n diagram (fig. 13, *left panel*). This causes a *decrease* in the mean pressure of the diffuse gas, and an *increase* in the mean pressure of the dense gas, because the point distribution is centered in the unstable range. For the dense gas, this furthermore causes a tendency towards producing flatter-topped histograms, because the fraction of high-pressure zones increases, but the short cooling time at those densities always produces a significant fraction (most frequently a majority) of points near $P_{\rm eq}$. Only for the case with the highest M and $k_{\rm for}$ does the peak of the pressure histogram for the dense gas shift to the high-P part of the histogram. Nevertheless, the fraction of zones in the simulations with $P \geq 10^4$ K cm^{-3} is seen to increase monotonically with either M or $k_{\rm for}$ (fig. 13, *right panel*). The fraction of the total number of cells with $n > 7.1$ cm^{-3} and $P \geq 10^4$ K cm^{-3} increases from 0.07% at $k_{\rm for} = 2$ and $M = 0.5$ to 69% at $k_{\rm for} = 16$ and $M = 1.25$.

In addition, larger rms Mach numbers are known to cause wider density PDFs (Padoan et al. 1997; Passot & Vázquez-Semadeni 1998), with the amplitude of the density fluctuations

depending on γ_e (Vázquez-Semadeni et al. 1996). As a consequence, wider pressure PDFs are also expected for stiffer-than-isobaric (i.e., $\gamma_e > 0$) behavior, in which the pressure is positively correlated with the density.

For the density PDF, Passot & Vázquez-Semadeni (1998; see also Scalo et al. 1998; Nordlund & Padoan 1999) showed that the density PDF is lognormal for isothermal flows ($\gamma_e = 1$; see also Vázquez-Semadeni 1994), but develops a power-law tail at high densities for $\gamma_e < 1$, and at low densities for $\gamma_e > 1$. A similar trend is also observed here in response to the resulting effective polytropic exponent: simulations with $k_{\rm for} = 2$ have $\gamma_e \lesssim 0.5$ (fig. 13, *left*), and their resulting density PDFs are skewed to the left, with shallower high-n tails that extend further from the PDF peak than the low-n side (fig. 11 *right*), although with signatures of the bimodality associated with the thermal bistability for the cases with the lowest-M. Instead, simulations with $k_{\rm for} = 16$, have density PDFs in which the low-n side is shallower and generally more extended, although again with signatures of bimodality on the high-n side at low M (fig. 12 *right*). Thus, the $k_{\rm for} = 2$ runs generally behave as if having $\gamma_e < 1$, while $k_{\rm for} = 16$ runs behave as if having $\gamma_e > 1$.

Interestingly, this dependence of the density PDF on γ_e is also apparent in the pressure histograms, and in fact it is even more pronounced, as can be seen in figs. 11 and 12 (*left panels*). This is somewhat surprising, given the large scatter of the P-n points in any given density interval. Naively, one would expect that such a large scatter would preclude any copying of the density-PDF features into the pressure histogram. Indeed, most features of the distribution do not survive the change of variable from density to pressure. This is the case of the scaling of the histogram width or the shift in position of the histogram peak with Mach number. Nevertheless, the development of a near power-law tail depending on the value of γ_e does seem to be preserved, and even amplified, in the pressure histogram.

5.2. Three-dimensional tests

The results from §§4.1 and 4.2 have been obtained in two-dimensional (2D) simulations exclusively, and it is thus important to determine whether these results are expected to persist in three dimensions (3D). The distinction between the 2D and 3D cases has been extensively discussed by Vázquez-Semadeni (1994) and Avila-Reese & Vázquez-Semadeni (2001). These authors have argued that the distinction is less pronounced in the highly compressible case, in which shocks are an important ingredient in the dynamics. This is because shocks are essentially one-dimensional structures, independently of the dimensionality of the global flow.

In order to confirm this expectation in the case of our particular problem, in this section

we present a comparison between selected cases in 2D and 3D, using simulations with 256 grid points in each direction. The 3D simulations are performed using a parallel version of the code. We first consider two simulations with $k_{\rm for} = 2$ and $M \sim 0.9$, one in 2D and the other in 3D. The precise Mach numbers are 0.90 and 0.85, respectively. Figure 14 shows the total histograms of pressure (*left*) and density (*right*). There we see that the pressure distribution of the 3D run is systematically shifted to higher values, by a factor $\lesssim 2$, with respect to that of the 2D one. On the other hand, the density distributions of the two runs coincide at high densities, but the 3D case has its peak and its low-density side again shifted to higher densities by about a factor of 2.

We speculate that these effects may be due to the fact that the density peaks are built by compressions of varying dimensionality, up to the dimensionality of the flow. The higher fraction of low-density regions in 2D can be understood as a consequence that a peak of a given average density and size contains a larger fraction of the total mass in 2D than in 3D. Thus, the "voids" surrounding the peaks are more heavily evacuated, giving a higher fraction of low-density zones and histograms that extend to lower values of the density. This typically lower density of the voids in 2D can also explain the typically lower values of the pressure at the low-pressure side of the distribution. On the other hand, for a density peak formed by a compression at a given characteristic velocity $\dot{R} \equiv dR/dt$, the density varies more rapidly in 3D than in 2D. That is, assume that $\rho \propto \mathcal{M} R^{-m}$, where $\mathcal{M}$ and R are respectively the mass and radius of the compressed parcel, and $m = 2$ in 2D and 3 in 3D. Then $\dot{\rho} = -m\mathcal{M} R^{-m-1}\dot{R}$, and the density rate of change is larger in 3D than in 2D at a given compression velocity $\dot{R}$. Thus, in 3D the characteristic time for variation of the density is comparatively shorter than the cooling time in 3D, and the behavior should be slightly closer to adiabatic, explaining the higher transient pressures in 3D at high densities.

Nevertheless, the differences in the histograms in 2D and 3D are relatively minor, probably because the occurrence of high-dimensional compressions must be a relatively rare event in comparison with one-dimensional ones (shocks). The pressure distribution in 3D is shifted by factors not larger than 2 in the 3D case, and in fact the P-n relation is very similar in the 2D and 3D cases, as seen from two-dimensional histograms in the pressure-density space (fig. 15), with the main difference being that the distribution of points in the 3D case extends slightly farther above the thermal equilibrium curve at densities $n \sim 1$ cm^{-3}. The least squares slopes of the distributions are also very similar, at 0.35 and 0.38 for 2D and 3D, respectively.

The trends described in previous sections for the pressure and density distributions resulting from 2D simulations as M and $k_{\rm for}$ are varied are also maintained in the 3D case. In fig. 16a and b we respectively show the pressure and density histograms resulting from

three simulations with $(M, k_{\rm for}) = (0.85, 2)$, $(0.90, 8)$, and $(1.35, 2)$. It can be observed that as $k_{\rm for}$ increases, the width of the pressure distribution and the value of $P(N_{\rm max})$ increase while the density histogram becomes narrower and with a less pronounced bimodality. On the other hand, when the value of M is increased, the pressure distribution widens noticeably, while the density distribution widens marginally; also, the bimodality of the latter is slightly less pronounced.

Finally, the fraction of cells with $n > 7.1$ cm^{-3} and $P \geq 10^4$ K cm^{-3} for the 3D simulation with $k_{\rm for} = 2$ and $M = 0.85$ is 1.3%, while that obtained in the 2D run with $k_{\rm for} = 2$ and $M = 0.97$ is 1.2%, again showing a high consistency between the 2D and 3D cases.

We conclude that the results obtained from the 2D simulations presented in §§4.1 and 4.2, as well as the discussion from §5.1, still hold in 3D.

5.3. Relation to previous work

Our results support the scenario that in a turbulent, thermally bistable flow, there exists a fraction of fluid parcels that are out of thermal equilibrium, and that this fraction depends on the local ratio η of the turbulent crossing time to the cooling time. Recently, Wolfire et al. (2003) have estimated this ratio for the warm neutral medium (WNM), using an approximation for the turbulent crossing time given by $t_{\rm shock} \sim \lambda_{\rm s}/c_{\rm s}$ (i.e., the "mean time between shocks"), where $c_{\rm s}$ is the sound speed and $\lambda_{\rm s}$ is the scale at which the typical turbulent velocity difference equals $c_{\rm s}$. We refer to $\lambda_{\rm s}$ as the "sonic" scale. Wolfire et al. (2003) estimated $\lambda_{\rm s} \sim 200$ pc for the WNM, and ~ 0.3 pc for the *cold* neutral medium (CNM), although they warned that this is a very uncertain quantity. With these estimates, they found $\eta \sim 0.3$–0.9 for the WNM, concluding that non-equilibrium temperatures should often be found in the WNM, in agreement with observations (Dickey et al. 1977; Kalberla et al. 1985; Spitzer & Fitzpatrick 1995; Fitzpatrick & Spitzer 1997; Heiles 2001; Heiles & Troland 2003; Kanekar et al. 2003) and previous numerical studies (Gazol et al. 2001).

This conclusion is also consistent with our present results. Adopting their value of ~ 200 pc for $\lambda_{\rm s}$, and a Kolmogorov velocity dispersion scaling law $\Delta v \propto \lambda^{1/3}$, appropriate for incompressible turbulence, we see that the rms Mach number with respect to the WNM at a scale of our simulation boxes (100 pc), should be $\sim 2^{-1/3} \approx 0.8$. Thus, based on their estimates, the WNM on scales of 100 pc should be bracketed by our simulations with $M = 0.5$ and $M = 1$, at the largest driving scales ($k_{\rm for} = 2$), with the $M = 1$ case being the most relevant.

However, it is possible that the above regime, arrived at through the considerations of Wolfire et al. (2003), still somewhat underestimates the role of turbulence. Those authors noted that, because of the scaling of the turbulent velocity with size, below the sonic scale the medium should roughly be in pressure equilibrium. However, this does not guarantee that thermal instability will be fully unimpeded in the generation of the density structures below this scale. As discussed by Vázquez-Semadeni et al. (2003), in a turbulent, thermally-bistable flow, there are three competing timescales: the sound crossing time $\tau_{\rm s}$, the turbulent crossing time $\tau_{\rm t}$, and the cooling time $\tau_{\rm c}$. In the standard linear analysis (Field 1965), the largest growth rate of the instability is given by the inverse of the cooling time, which is independent of scale in the linear regime. This largest growth rate occurs at an intermediate-wavelength regime $\lambda_{\rm F} \ll \lambda \lesssim \lambda_{\rm eq}$, where $\lambda_{\rm F}$ is the Field length and $\lambda_{\rm eq}$ is the scale at which $\tau_{\rm s} \sim \tau_{\rm c}$ (c.f. §5.1). On the other hand, the sound and turbulent crossing times do depend on scale, with $\tau_{\rm s} \propto \lambda$ and $\tau_{\rm t} \propto \lambda^{2/3}$ (assuming an incompressible Kolmogorov spectrum), or $\tau_{\rm t} \propto \lambda^{1/2}$ (assuming a highly compressible, Burgers-like spectrum, appropriate for the unstable range). So, even though indeed the ratio of sound-to-turbulent crossing times becomes progressively smaller with decreasing scale size, the ratio $\eta \equiv \tau_{\rm t}/\tau_{\rm c}$ also becomes smaller. This suggests that nearly incompressible, shearing turbulent fluctuations may have time to disrupt TI-induced condensations before they grow, at least partially. This effect may be enhanced in the presence of magnetic fields, which increase the solenoidal (shearing) fraction of the turbulent kinetic energy (Vázquez-Semadeni et al. 1996). Indeed, even in our weakest-turbulence (largest-η) simulations ($M = 0.5$, $k_{\rm for} = 2$), the bimodality of the density PDF (caused by the thermal bistability) is moderate (fig. 11 *right panel*), and the global effective polytropic exponent is already positive across the thermally unstable range (fig. 13, *left panel*)).

Our results also have the implication that the development of a high-P power-law tail is not exclusive to supernova-driven models, such as the McKee & Ostriker (1977) model, and that pure advective driving can generate approximate power-law tails in low-$\gamma_{\rm e}$ flows at sufficiently high Mach numbers. On the other hand, noting that we also obtain lognormal-like shapes in the high-P sides of the PDFs for large $k_{\rm for}$ suggests that the formation (or not) of power-law tails in the pressure PDF depends on $\gamma_{\rm e}$.

Finally, the fact that the pressure histogram partially copies features of the density histogram, in particular the production of power-law tails as a function of $\gamma_{\rm e}$, gives validation to the approach used by Mac Low et al. (2004), who applied a change of variable from density to pressure in order to understand the functional form of the pressure PDF from the known shape of the density PDF. On first account, such a procedure might be questioned because of the large scatter exhibited by the pressure at any given density, but our results suggest that it may be valid on average.

Observationally, Jenkins (2004) has recently presented histograms of the pressure in observations of CI, which can in principle be compared with our results, as well as with pressure histograms from full ISM simulations, like those of Mac Low et al. (2004) and de Avillez & Breitschwerdt (2004). However, at this point such a comparison is ambiguous, because Jenkins (2004) had to *assume* an effective polytropic exponent in order to correct for an over-representation of dense points in his observational sample. Since our results indicate that $\gamma_{\rm e}$ determines the shape of the pressure histogram, it appears difficult to disentangle this physical role of $\gamma_{\rm e}$ from its possible role in biasing the observed pressure distribution. A detailed attempt to perform such a comparison will be presented elsewhere, but here we just note that our fraction of points with $P \geq 10^4$ K cm^{-3} for the case $M = 0.5$, $k_{\rm for} = 2$, of order 0.07%, appears consistent with the fraction reported by Jenkins (2004) for approximate thermal equilibrium in the cold medium, also $\sim 0.1\%$.

6. Conclusions

In this paper we have carried out a systematic study of the effect of turbulent velocity fluctuations, characterized by their rms Mach number M and the energy injection wavenumber, $k_{\rm for}$, on the thermal pressure distribution in a thermally bistable flow. To this end we have performed a large number of 2D simulations varying those two parameters in 100-pc boxes with random turbulent driving generated in Fourier space, which allows precise control of the parameters. A few test cases in 3D suggest that the 2D results are valid in 3D as well. Our results are consistent with the picture that as either of these parameters is increased, the ratio of turbulent crossing time to cooling time decreases, causing a departure from thermal equilibrium, and an approach towards an *adiabatic* behavior. This translates into an increase of the effective polytropic index $\gamma_{\rm e}$, as measured by the slope of the distribution of points in the pressure-density diagram, in turn creating a population of underpressured zones in the diffuse gas, and of overpressured zones in the dense gas, with respect to the thermal-equilibrium value of the pressure, $P_{\rm eq}$. In particular, the fraction of zones with densities $n > 7.1$ cm^{-3} and with $P > 10^4$ K cm^{-3} increases from roughly 0.1% at $k_{\rm for} = 2$ (a driving scale of 50 pc) and $M = 0.5$ to roughly 70% for $k_{\rm for} = 16$ (a driving scale of 6.25 pc) and $M = 1.25$. In particular, for $M = 1$ and $k_{\rm for} = 2$, this fraction is $\sim 1\%$, similar to the value reported by Jenkins (2004) from a survey of the fine-structure excitation of CI on the Glactic plane.

In all cases, the dynamic range of the pressure in any given density interval is larger than one order of magnitude, and the total dynamic range, summed over the entire density range, typically spans 3–4 orders of magnitude. The total pressure histogram widens as the

Mach number is increased, and moreover develops near-power-law tails at high (resp. low) pressures when $\gamma_e \lesssim 0.5$ (resp. $\gamma_e \gtrsim 1$), which occurs at $k_{for} = 2$ (resp. $k_{for} = 16$) in our simulations. The opposite side of the pressure histogram decays rapidly, in an approximately lognormal form. The development of power-law tails in the pressure PDF is analogous to, and in fact more pronounced than, that observed in the density PDF, suggesting that the average value of the pressure is sufficiently correlated with the density as to reflect the same dependence of its histogram with γ_e, in spite of the large scatter of the pressure at any given density. This may validate approaches attempting to obtain the pressure PDF from that of the density via a change of variables.

We would like to acknowledge E. B. Jenkins and P. Hennebelle for useful comments and thank an anonymous referee for suggestions to improve this work. This work has received partial financial support from CONACYT grant 36571-E to E. Vázquez-Semadeni and from DGAPA grant PAPIIT-IN114802 to A. Gazol. The work of J. Kim was supported by the Astrophysical Research Center for the Structure and Evolution of the Cosmos (ARCSEC) of Korea Science and Engineering Foundation (KOSEF) through the Science Research Center (SRC) program. The numerical simulations were performed on the linux clusters at CRyA (funded by CONACYT grant 36571-E) and at KAO (funded by KAO and ARCSEC). This work has made extensive use of NASA's Astrophysics Abstract Data Service and LANL's astro-ph archives.

REFERENCES

Audit, E. & Hennebelle P. 2004,A&A, in press

Avila-Reese, V., & Vázquez-Semadeni E. 2001, ApJ, 553, 645

Begelman, M. C., & McKee, C. F. 1990, ApJ, 358, 375

Burkert, A., & Lin, D. N. C. 2000, ApJ, 537, 270

Cox, D. P., & Smith, B. W. 1974, ApJ, 189, L105

de Avillez, M. A., & Breitschwerdt, D. 2004, astro-ph/0407034

Dickey, J. M., Salpeter, E. E.& Terzian, Y. 1977, ApJ, 211, L77

Field, G. B. 1965, ApJ, 142, 531

Field, G. B., Goldsmith, D. W., & Habing, H. J. 1969, ApJ, 155, L149

Fitzpatrick, E. L. & Spitzer, L. ApJ, 475, 623

A. Gazol, A., Vázquez-Semadeni, E., Sánchez-Salcedo, F. J.& Scalo, J. M. 2001 ApJ, 557, 121

Harten, A., Lax, P. D., & van Leer, B. 1983, SIAM, Rev., 25, 35

Heiles, C. 2001, ApJ, 551, L105

Heiles, C. & Troland, T. 2003, ApJ, 586, 1067

Hennebelle, P., & Pérault, M. 1999, A&A, 351, 309

Hennebelle, P., & Pérault, M. 2000, A&A, 359, 1124

Jenkins, E. B. 2002, ApJ, 580, 938

Jenkins, E. B. 2004, ApSS 289, 215 (Proceedings of From Observations to Self-Consistent Modelling of the ISM in Galaxies, eds. M. de Avillez & D. Breitschwerdt (Dordrecht: Kluwer))

Jenkins, E. B., Jura, M. & Lowenstein, M. 1983, ApJ, 270, 88

Jenkins, E. B. & Tripp, T. M. 2001, ApJ, 137, 297

Kanekar, N., Subrahmanyan, R., Chengalur, J. N., & Safouris, V. 2003, MNRAS, 346, L57

Kim et al. 1999 Kim, J., Ryu, D., Jones, T. W., & Hong, S. S. 1999, ApJ, 514, 506

Korpi, M. J., Brandenburg, A., Shukurov, A., Tuominen, I., & Nordlund, A. 1999, ApJ, 514, 99L

Koyama, H., & Inutsuka, S.-I. 2000, ApJ, 532, 980

Koyama, H., & Inutsuka, S.-I. 2002, ApJ, 564, L97

Koyama, H., & Inutsuka, S.-I. 2004, ApJ,

Kritsuk, A., & Norman, M.L. 2002, ApJ, 569, L127

Lang, K. R. *Astrophysical Formulae vol. I*, 3th edn., (Springer-Verlag, Berlin, 1999)

Mac Low, M.-M. 1999, ApJ 524, 169

Mac Low, M. M., Balsara, D., & Kim, J., Avillez, M. A. 2004, ApJ submitted (astro-ph/0410734)

Mac Low, M. M., & Klessen, R. S. 2004, Rev. Mod. Phys., 76, 125

McKee, C.F. & OstrikerJ.P. 1977, ApJ, 218, 148

Meerson, B. 1996, Rev. Mod. Phys., 68, 215

Nordlund, Å., & Padoan, P. 1999, in Interstellar Turbulence, eds. J. Franco and A. Carramiñana (Cambridge: Cambridge University Press), p. 218

Norman, C. A. Ferrara, A. 1996, ApJ467, 280

Padoan, P. Nordlund, A., & Jones, 1998, MNRAS, 299, 123

Passot, T., & Vazquez-Semadeni, E. 1998, Phys. Rev. E 1999, 58, 4501

Piontek, R. A., & Ostriker, E. C. 2004, ApJ, 601, 905

Redfield, S. & Linsky J. L. 2004, ApJ, 613, 1004

Sánchez-Salcedo, F. J., Vázquez-Semadeni, E., & Gazol, A. 2002, ApJ, 577, 768

Scalo, J. M. 1987 Interstellar processes; Proceedings of the Symposium, Grand Teton National Park, WY, July 1-7, 1986. Dordrecht, D. Reidel Publishing Co. p.349-392

Scalo, J., Vázquez-Semadeni, E., Chappell, D., & Passot, T. 1998, ApJ, 504, 835

Spitzer, L. & Fitzpatrick E. L. 1995, ApJ, 445, 196

Toro, E. F. 1999, Riemann Solvers and Numerical Methods for Fluid Dynamics: A practical Introduction (Berlin: Springer)

Vázquez-Semadeni E. 1994, ApJ, 423, 681

Vázquez-Semadeni E. 2002 in Seeing Through the Dust: The Detection of HI and the Exploration of the ISM in Galaxies, ASP Conference Proceedings, Vol. 276. Edited by A. R. Taylor, T. L. Landecker, and A. G. Willis. San Francisco: Astronomical Society of the Pacific, p.155

Vázquez-Semadeni, E., Gazol, A., & Scalo, J. 2000, ApJ, 540, 271

Vázquez-Semadeni, E., Gazol, A., Sánchez-Salcedo, F. J., and Passot, T. ed. Thierry Passot & Edith Falgarone, 2003, Lecture Notes in Physics, vol. 614, p.213-251

Vázquez-Semadeni E., Passot T., & Pouquet A., 1995, ApJ, 441, 702

Vázquez-Semadeni E., Passot T., & Pouquet A., 1996, ApJ, 473, 881

Wolfire, M. G., McKee, C. F., Hollenbach, D., & Tielens, A. G. G. M. 2003, 587, 278

Wolfire, M. G., Hollenbach, D., McKee, C. F., Tielens, A. G. G. M. & Bakes, E. L. O. 1995, ApJ, 443, 152

This preprint was prepared with the AAS LaTeX macros v5.2.

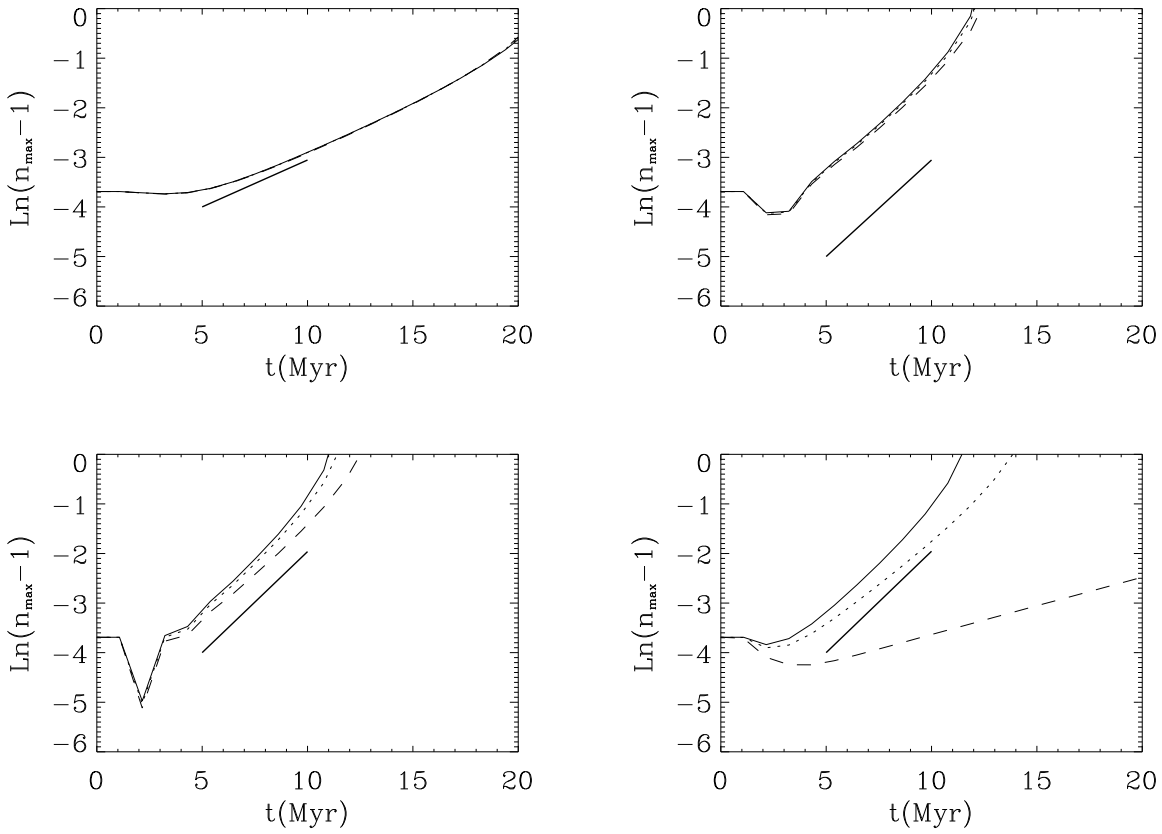

Fig. 1.— Temporal growth of sinusoidal density perturbations with an initial amplitude of 2.5% and a period of 50 pc (*upper left*), 25 pc (*upper right*) 12.5 pc (*lower left*) and 6.25 pc (*lower right*). The *dashed*, *dotted* and *solid* lines correspond to resolution of 256^2, 512^2 and 1024^2, respectively. The thick straight lines indicate the slope of the theoretical growth rate at the corresponding scale.

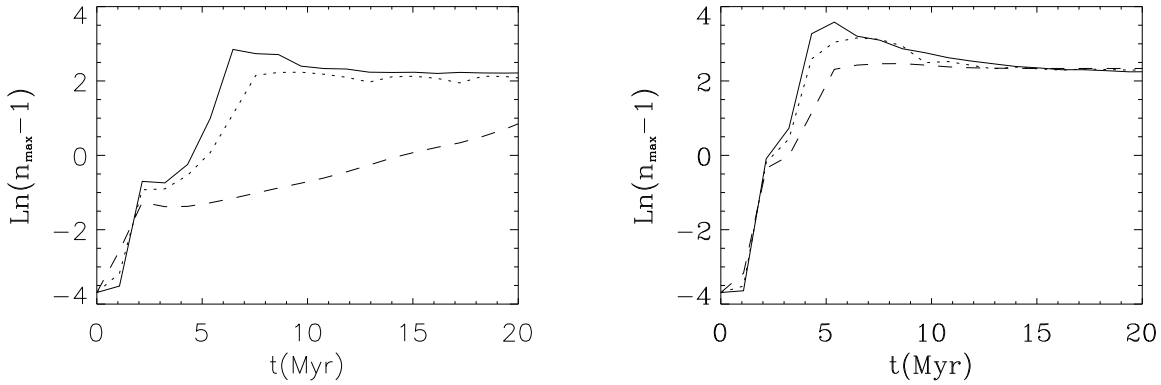

Fig. 2.— Temporal growth of sinusoidal density perturbations with an initial amplitude of 2.5% and a period of 6.25 pc (*left*) and 12.5 pc (*right*) for simulations including an initial velocity perturbation at amplitude equivalent to Mach number $M = 1.0$ with respect to the unstable medium at $T = 2400$ K. The *dashed*, *dotted* and *solid* lines correspond to resolutions of 256^2, 512^2 and 1024^2, respectively.

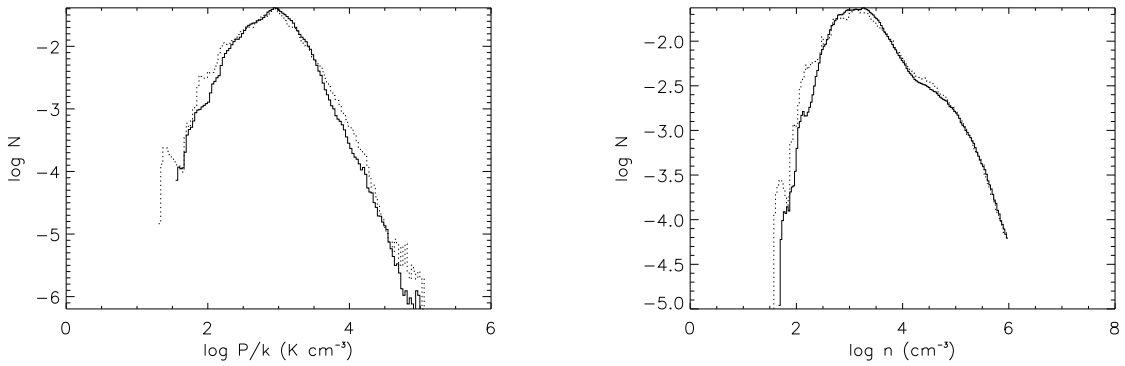

Fig. 3.— Comparison of the total pressure (*left*) and density (*right*) histograms for simulations with resolutions 512^2 (*dotted lines*) and 1024^2 (*solid lines*). The histograms are normalized to the total number of points, and averaged over the time interval $1.1 \leq t \leq 2$, where the time unit is the simulation sound crossing time at $T = 10^4$ K

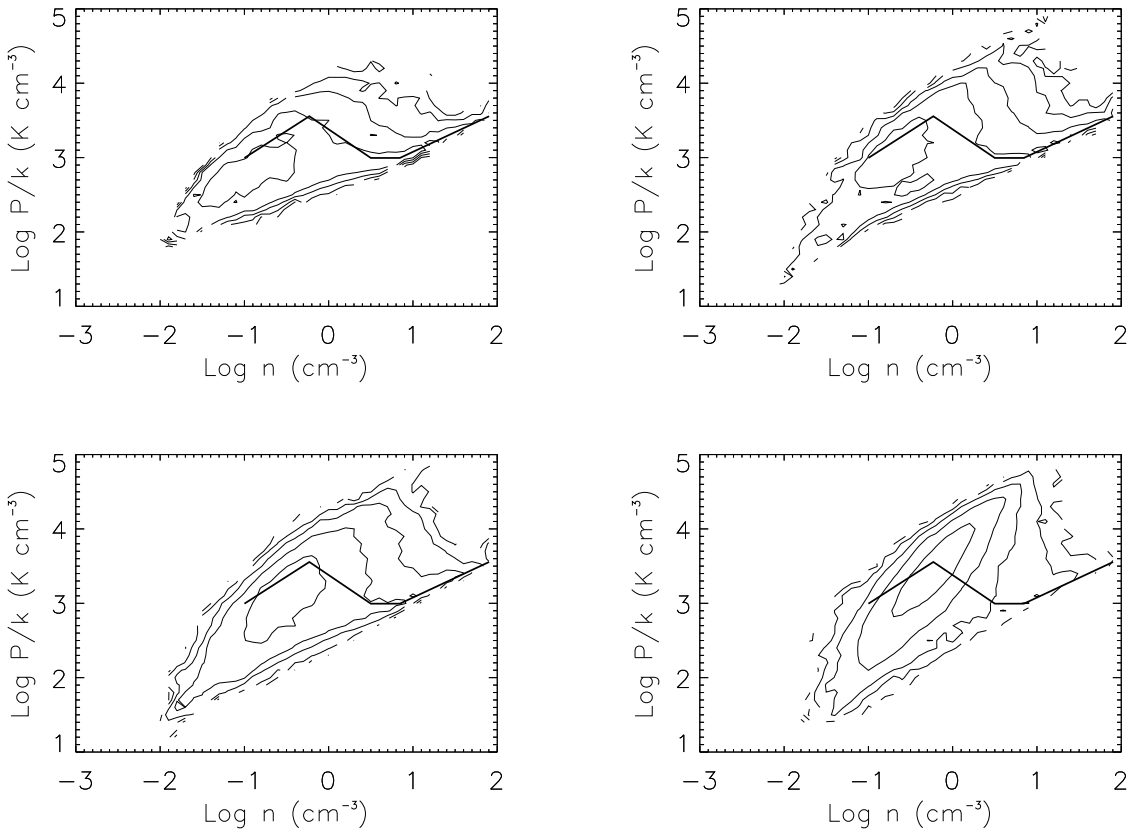

Fig. 4.— Thermal pressure-density relation for simulations with $M \sim 1$ and $k_{\rm for} = 2$ (*upper left*), $k_{\rm for} = 4$ (*upper right*), $k_{\rm for} = 8$ (*lower left*) and $k_{\rm for} = 16$ (*lower right*). The solid line in each panel denotes the thermal-equilibrium pressure.

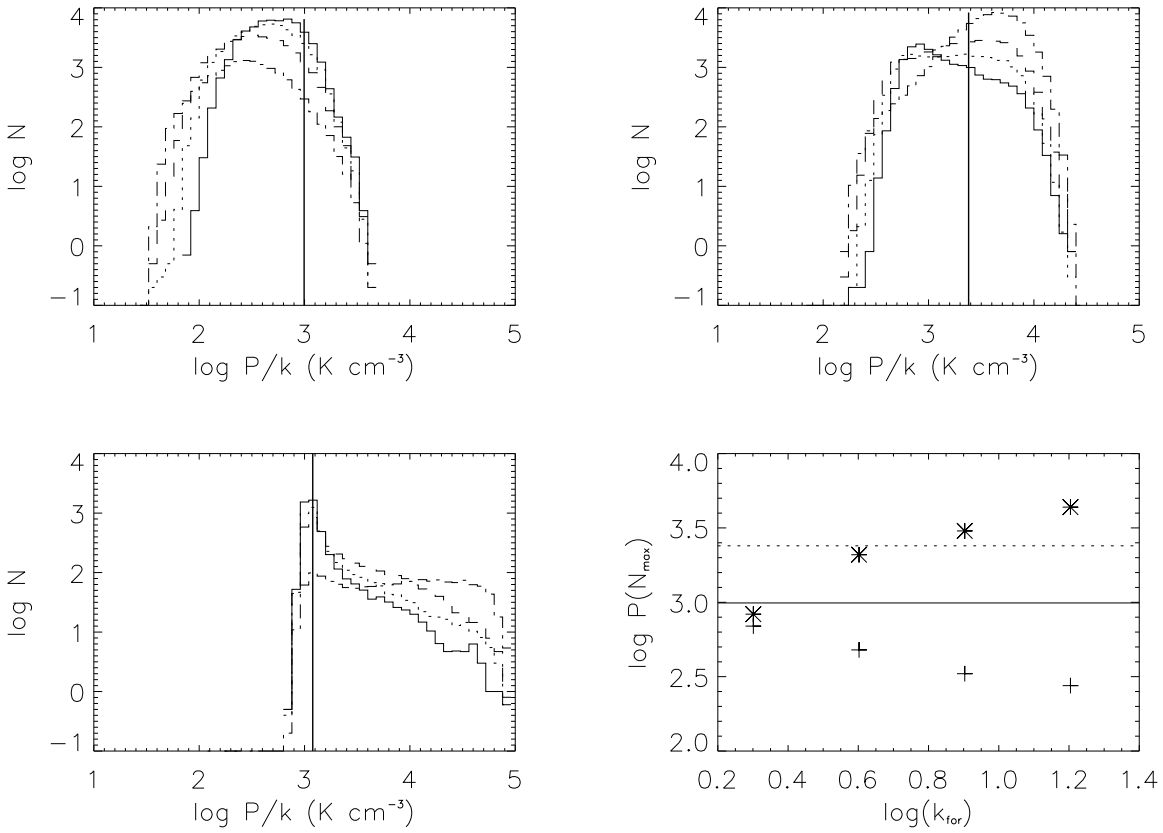

Fig. 5.— Temporally-averaged pressure histograms for simulations with $M \sim 1$ and $k_{\rm for} = 2$ (*solid line*), $k_{\rm for} = 4$ (*dotted line*), $k_{\rm for} = 8$ (*dashed line*) and $k_{\rm for} = 16$ (*dashed-dotted line*). The time averaging is as in fig. 3. The histograms are computed over logarithmic density intervals $n_c/\sqrt{2} \leq n_c \leq \sqrt{2}n_c$, centered at $n_c = 0.1$ cm^{-3} (*upper left panel*), $n_c = 1.0$ cm^{-3} (*upper right panel*), and $n_c = 10.0$ cm^{-3} (*lower left panel*). The vertical lines denote the thermal-equilibrium pressure P_{eq} at n_c. *Lower right panel*: most probable pressure $P(N_{\rm max})$ for the histograms centered on $n_c = 0.1$ cm^{-3} (*plus signs*) and $n_c = 1.0$ cm^{-3} (*asterisks*). The horizontal lines denote the values of $P_{eq}(n_c = 0.1$ cm$^{-3})$ (*solid line*) and $P_{eq}(n_c = 1$ cm$^{-3})$ (*dotted line*).

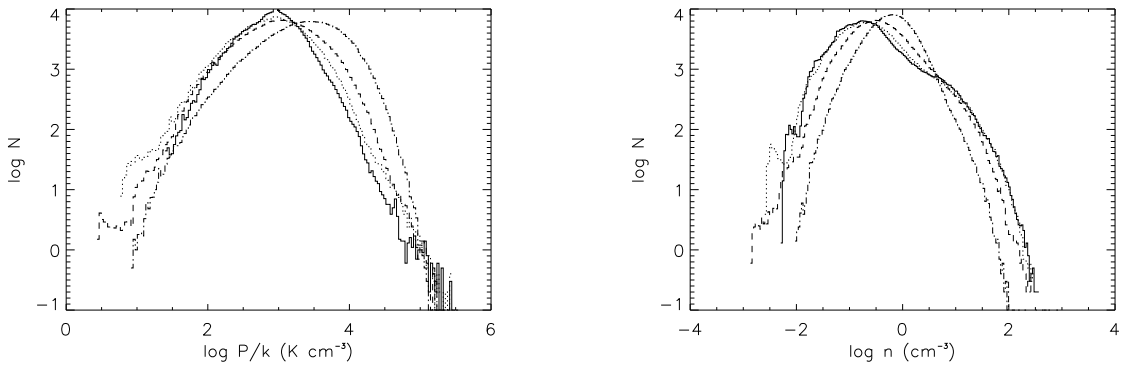

Fig. 6.— Total pressure (*left*) and density (*right*) histograms for simulations with $M \sim 1$ and $k_{\rm for} = 2$ (*solid line*), $k_{\rm for} = 4$ (*dotted line*), $k_{\rm for} = 8$ (*dashed line*) and $k_{\rm for} = 16$ (*dashed-dotted line*). The histograms are time-averaged as in fig. 3.

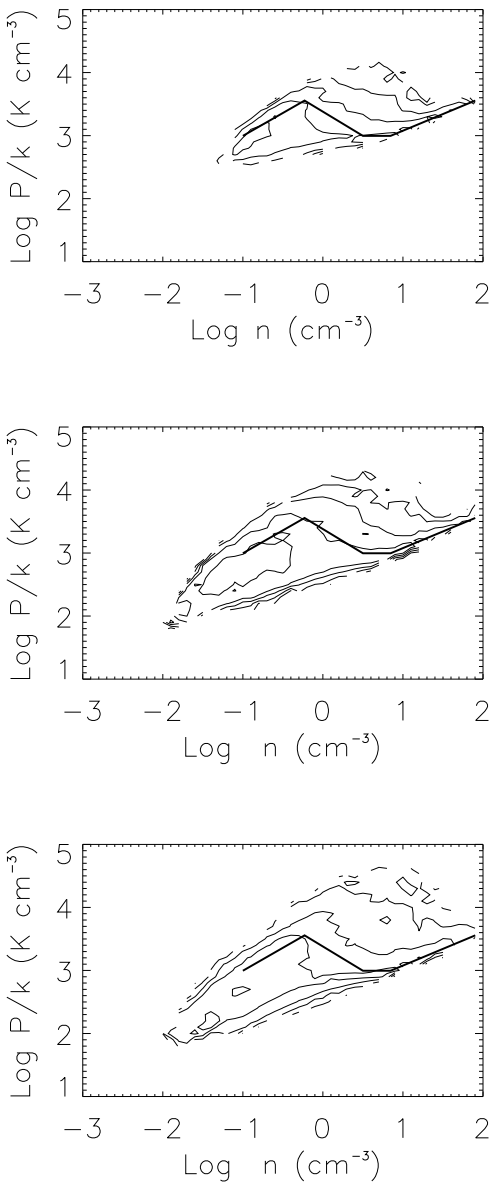

Fig. 7.— Thermal pressure-density relation for simulations with $k_{\rm for} = 2$ and $M \sim 0.5$ (*upper panel*), $M \sim 1$ (*center panel*) and $M \sim 1.25$ (*lower panel*). The solid line in each panel shows the thermal-equilibrium pressure.

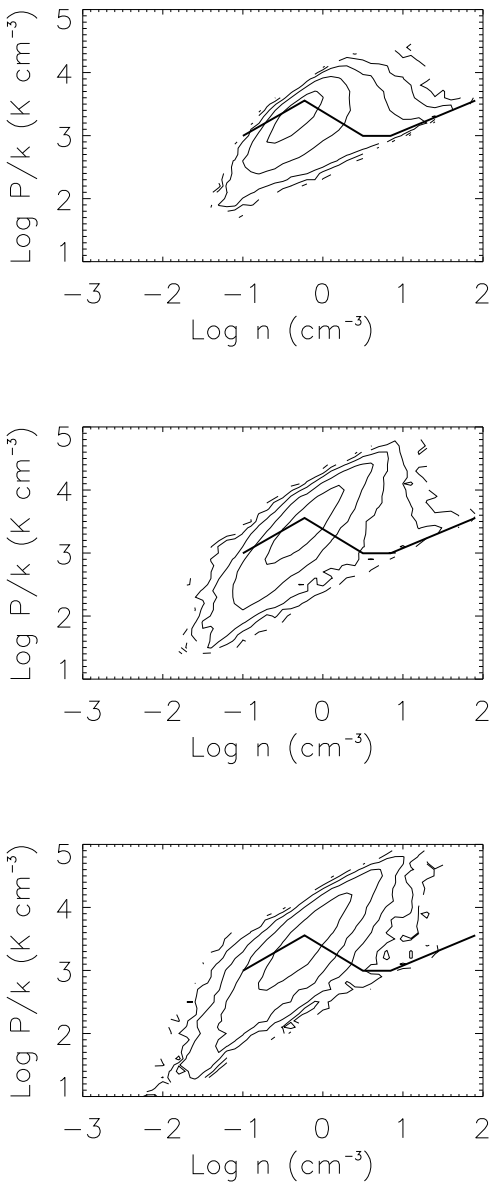

Fig. 8.— Thermal pressure-density relation for simulations with $k_{\rm for} = 16$ and $M \sim 0.5$ (*upper panel*), $M \sim 1$ (*center panel*) and $M \sim 1.25$ (*lower panel*). The solid line in each panel shows the thermal-equilibrium pressure.

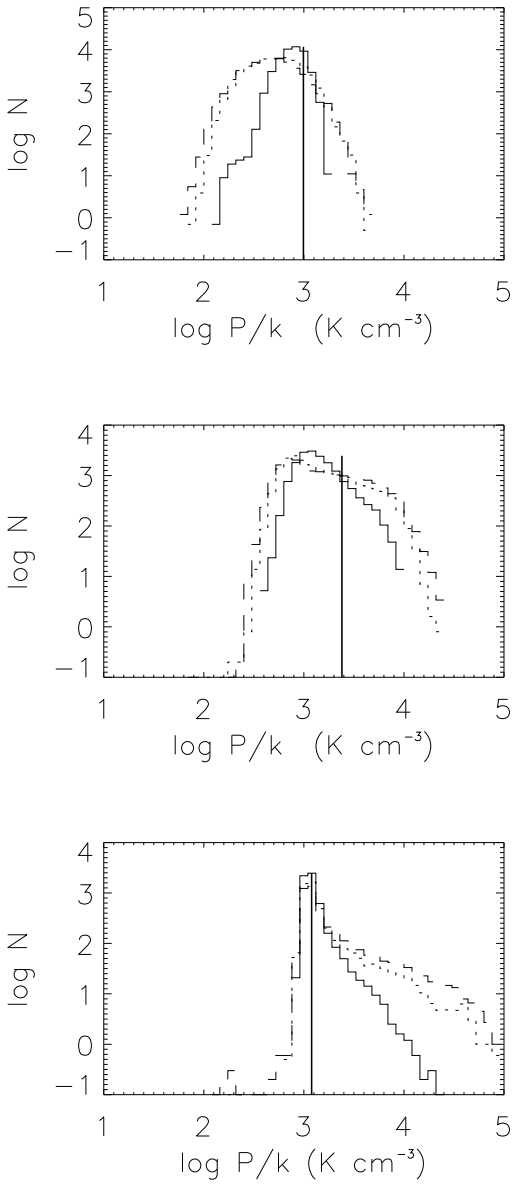

Fig. 9.— Pressure histograms over specific density intervals as in fig. 5, but for simulations with $k_{\rm for} = 2$ and $M \sim 0.5$ (*solid line*), $M \sim 1.0$ (*dotted line*), and $M \sim 1.25$ (*dashed line*).

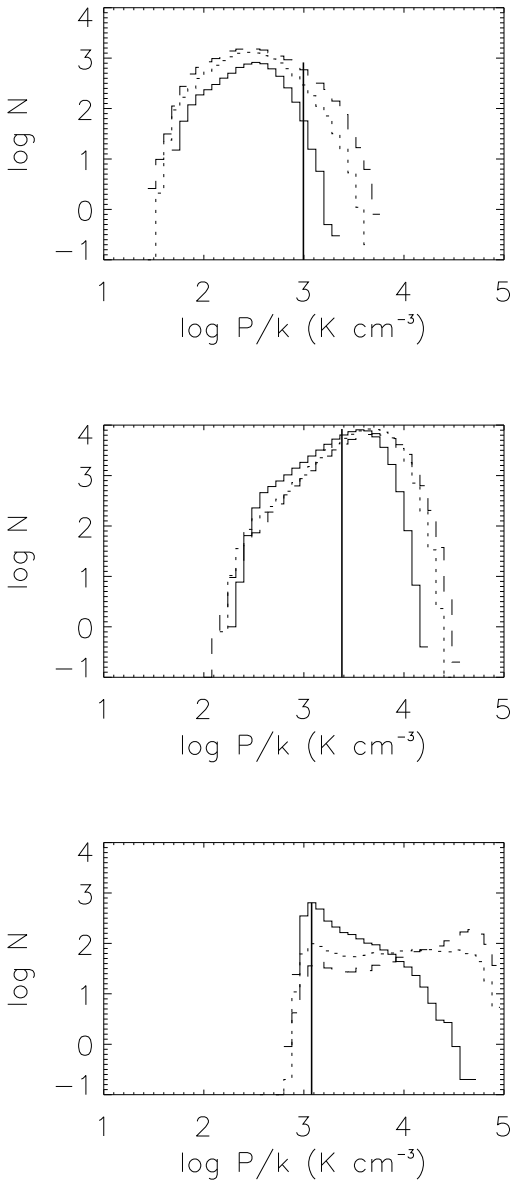

Fig. 10.— Pressure histograms over specific density intervals as in fig. 5, but for simulations with $k_{\rm for} = 16$ and $M \sim 0.5$ (*solid line*), $M \sim 1.0$ (*dotted line*).

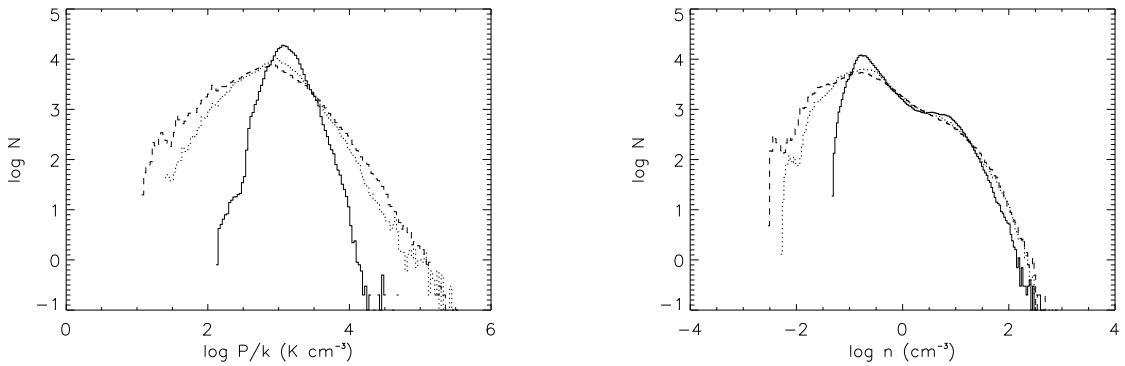

Fig. 11.— Total time-averaged pressure (*left*) and density (*right*) histograms as in fig. 6 but for simulations with $k_{\rm for} = 2$ at $M \sim 0.5$ (*solid line*), $M \sim 1.0$ (*dotted line*), and $M \sim 1.25$ (*dashed line*).

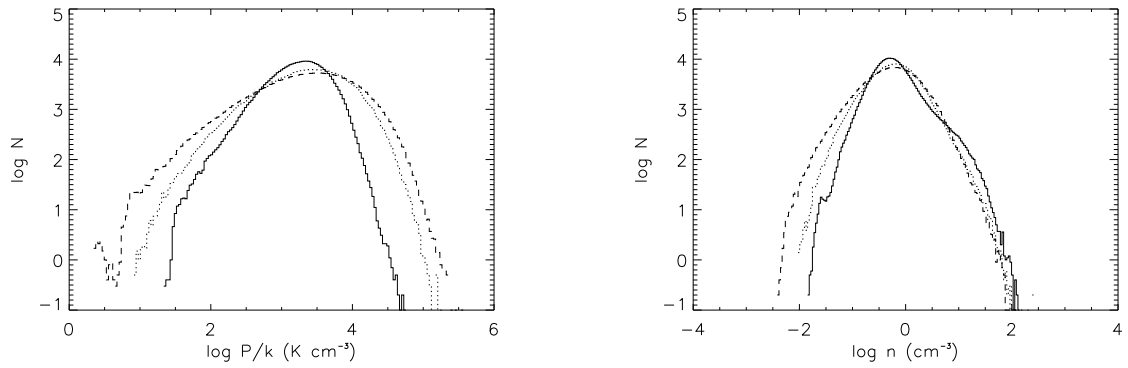

Fig. 12.— Temporally-averaged pressure (*left*) and density (*right*) histograms as in fig. 6 but for simulations with $k_{\rm for} = 16$ and $M \sim 0.5$ (*solid line*), $M \sim 1.0$ (*dotted line*), and $M \sim 1.25$ (*dashed line*).

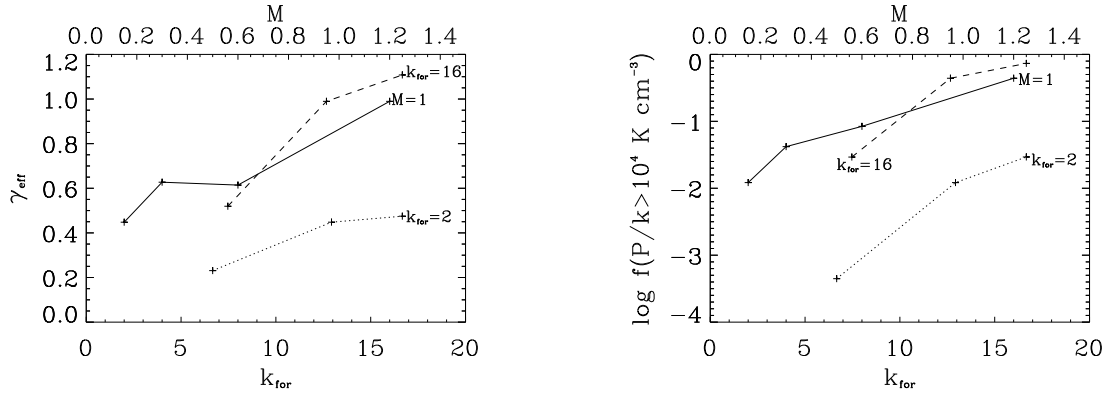

Fig. 13.— *Left:* Least squares slope of the distributions of points in figs. 4, 7 and 8. The *solid* line shows the variation with the driving wavenumber $k_{\rm for}$, indicated by the lower horizontal axis, at fixed rms Mach numbers $M = 1$. The *dotted* and *dashed* lines show the variation with M, indicated by the upper horizontal axis, at a given $k_{\rm for}$, indicated by the label next to each line. *Right:* Fraction of grid cells with $P > 10^4$ K cm^{-3} and for the $n > 7.1$ cm^{-3} in figs. The line coding is as in the *left* panel.

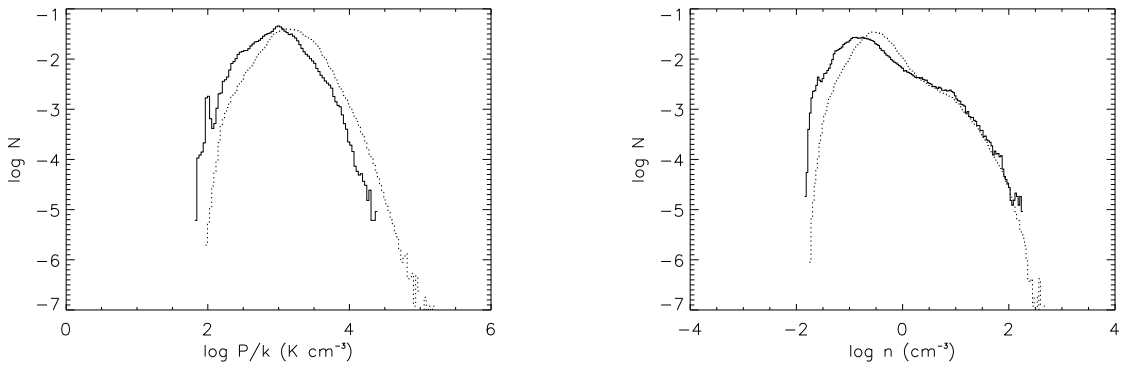

Fig. 14.— Pressure (*left*) and density (*right*) histograms for simulations with $k_{\rm for} = 2$ and $M = 0.90$ in 2D (*solid line*), and $M = 0.85$ in 3D (*dotted line*). The histograms are normalized to the total number of points and for the 2D simulations they are averaged over the time interval $3.2 < t/t_0 < 4$.

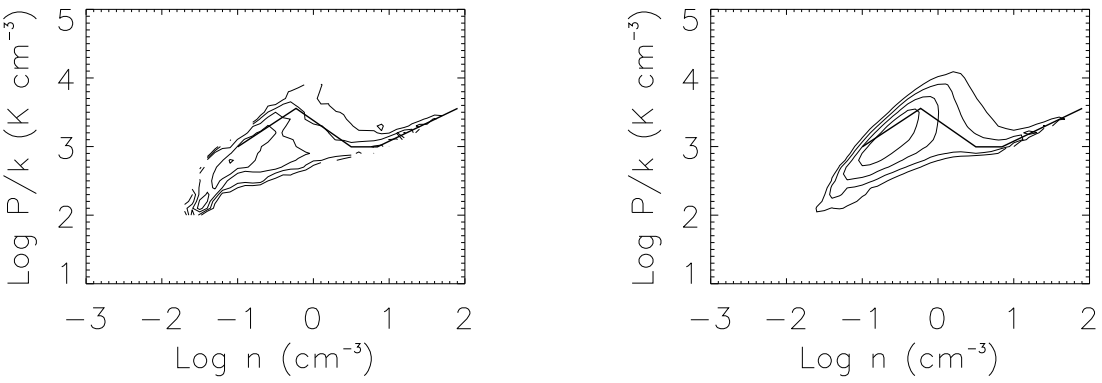

Fig. 15.— Thermal pressure-density relation for three-dimensional simulations with $k_{\rm for} = 2$ and $M = 0.90$ in 2D (*left panel*) and $M = 0.85$ in 3D (*right panel*). The solid line in each panel shows the thermal-equilibrium pressure.

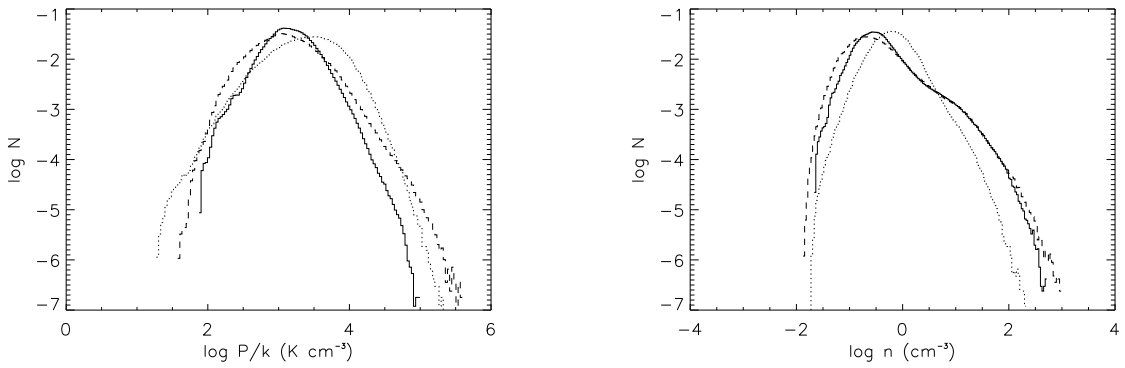

Fig. 16.— Total pressure (*left*) and density (*right*) histograms for 3D simulations with $M = 0.85$ and $k_{\rm for} = 2$ (*solid line*), $M = 0.85$ and $k_{\rm for} = 8$ (*dotted line*), and $M = 1.35$ and $k_{\rm for} = 2$ (*dashed line*). The histograms are normalized to the total number of points.